Full Length Article

Concurrent photocatalytic degradation of organic contaminants and photocathodic protection of steel Ag–TiO$_2$ composites

Robert Liang [a,b,*], Olivia M. Schneider [a], Nathan Lun [a], Pablo D. Enrique [a], Dulal C. Saha [a], Lena C.M. Li Chun Fong [a], Ivana Jaciw-Zurakowsky [a], Mark R. Servos [c], Peng Peng [d], Norman Y. Zhou [a,b]

[a] *Department of Mechanical and Mechatronics Engineering, Centre for Advanced Materials Joining, University of Waterloo, 200 University Ave. W., Waterloo, Ontario, N2L 3G1, Canada*
[b] *Waterloo Institute of Nanotechnology, University of Waterloo, 200 University Ave. W., Waterloo, Ontario, N2L 3G1, Canada*
[c] *Department of Biology, University of Waterloo, 200 University Ave. W., Waterloo, Ontario, N2L 3G1, Canada*
[d] *School of Mechanical Engineering and Automation, International Research Institute for Multidisciplinary Science, Beihang University, 37 Xueyuan Rd, Beijing, 100191, China*

ARTICLE INFO

ABSTRACT

In this study, coupled titanium dioxide-silver composite and steel electrode pairs were investigated for their use in cathodic protection under illuminated and dark conditions to prevent corrosion and enhance contaminant degradation under photocatalysis. A series of photoelectrochemical tests were used to determine the properties of the photoanode and identify the cathodic protection behaviour in the presence and absence of organic/inorganic contaminants. Additionally, corrosion-prone steel was used to test the principle of photocathodic protection in reducing oxide formation and mass loss under base metal and welded materials.

1. Introduction

Stainless steel is often the material of choice in construction because it forms a passive film that protects the metal from corrosion. However, corrosion is still a concern in moist chloride-containing environments, which break down the protective film. Stainless steel components that are at an increased risk of corrosion include crevices (which allow chloride accumulation), nuts and bolts (galling), manufacturing defects and reduced oxygen environments (pitting), and welded regions (which show decreased corrosion resistance in heat affected zones). This limits utility in a variety of industrial and construction applications. Marine applications in particular are limited due to the inherent corrosivity of seawater [1–3]. Because of the lack of suitable materials available, costly repairs and replacements must be made regularly.

One potential solution is the application of a coating to protect from corrosion. Unfortunately these coatings scratch easily, reducing their lifetime and durability [4–7]. Another potential solution is cathodic pro-

tection, where a sacrificial anode supplies electrons to reduce the rate of reactions at the stainless steel. Because the anode is sacrificial it requires regular replacement, which adds additional maintenance costs [8].

Photocathodic protection is a variation on the traditional cathodic protection which uses a photocatalytic anode to generate electrons. This photoanode is advantageous because it is not consumed and so it doesn't need to be replaced. A common photoanode material is nano titanium dioxide, which produces electrons when exposed to light [9–11]. In previous work, TiO$_2$ has also shown the added benefit of photocatalytically degrading contaminants in solution [12–17]. The drawbacks of TiO$_2$ are that it requires ultraviolet (UV) light, and rapidly undergoes charge recombination. To improve upon the photocathode's performance, a hole scavenger such as Na$_2$S can be added to reduce recombination. Metal nanoparticles (NPs) such as gold, platinum, and silver can also be imbedded to improve the performance [18–21]. Ag NPs are most commonly used because they are cheaper than other noble metal NPs [22]. The

drawback is that Ag NPs readily corrode in the presence of oxygen, sulphides, and chlorides (forming silver oxide, silver sulphide, and silver chloride respectively), which are the most environmentally relevant corrosive agents for Ag [23]. Ag also oxidizes readily under photocathodic conditions [24,25]. The addition of a SiO_2 coating over the Ag NPs greatly improves the corrosion resistance of the material by providing a passive physical barrier, which is unreactive with the agents that corrode Ag under typical conditions [26,27].

In this work, electrophoretic deposition was used to deposit Ag NP core encapsulated in a silica-titania shell (AST) combined with commercial TiO_2 powder onto fluoride tin oxide conductive glass. The coated glass served as photoanodes and were used to investigate the cathodic protection of stainless steel under xenon lamp illumination to simultaneously prevent corrosion and enhance contaminant degradation under photocatalysis. The elemental map and morphology of the thin films composites were determined and the influence of AST on the photoelectrochemical properties were determined, in the presence of both organic and inorganic contaminants. Additionally, corrosion sensitive steel – both base metal and welded material – was used to inspect corrosion product formation at a short timescale through mass loss analysis and oxide peak identification.

2. Materials and methods

2.1. Reagents and chemicals

3-Aminopropyltrimethoxysilane (APTMS), titanium tetraisopropoxide (TTIP), acetylacetone, polyvinylpyrrolidone (PVP K30), P25 Aeroxide^{TM}, iodine, glucose, disodium sulfite (Na_2S), and FTO coated glass (with a surface resistivity of 15 Ω cm^{-2}) were purchased from Sigma-Aldrich. Silver nitrate and tetra orthosilicate (TEOS) were purchased from Alfa-Aesar. Titanium metal sheets (grade 2) and stainless steel (SS304) were purchased from McMaster Carr. Corrosion-prone steel (Usibor® 22MNB5) sheets were supplied by Dofasco.

2.2. Synthesis of Ag@SiO₂–TiO₂ NPs

The synthesis of Ag@SiO₂–TiO₂ (AST) NPs is as described in previous work [28]. Briefly, AgNO₃ and PVP were dissolved in ethylene glycol and heated to 130 °C for 0.5 h under 600 rpm, then left for 1 h without stirring to form Ag NPs. The Ag NPs were isolated from the ethylene glycol and re-dispersed in ethanol to obtain a concentration of about 6.0 g L^{-1}.

The Ag@SiO₂ NPs were formed using a procedure described elsewhere [29]. In summary, 50 mL of Ag NPs in ethanol was further diluted in an additional 120 mL of ethanol and stirred at room temperature for 0.5 h at 600 rpm. 40 mL of deionized water and 2.4 mL aqueous ammonia (28 wt%) were then added. 50 μL TEOS diluted in 10 mL ethanol was added dropwise with continuous stirring, then stirred for 10 h. The resulting Ag@SiO₂ core-shell NPs were first washed once with water and three times with ethanol, then re-dispersed in 50 mL of ethanol.

The 50 mL of Ag@SiO₂ NPs was further diluted in 70 mL of ethanol and 200 μL APTMS was added, then the solution was refluxed at 85 °C for 6 h. The APTMS-modified Ag@SiO₂ NPs were washed with ethanol three times and re-dispersed in 200 mL of ethanol. 200 μL of TTIP diluted in 40 mL of ethanol was added dropwise to the APTMS-modified Ag@SiO₂ dispersion with stirring, then refluxed at 85 °C for 3 h. The resulting AST NPs were washed well with water and then dried overnight at 60 °C.

2.3. The preparation of photoanodes

The preparation of the photoanodes was done using a electrophoretic method described previously [28]. Briefly, to make 1% Ag@SiO₂–TiO₂/P25 composites (AST-P25), P25 and AST NPs in ethanol were sonicated. The beaker containing this solution was then placed in a larger beaker containing the following electrophoretic bath mixture: 1×

methanol, 1.4× ethanol, 0.4× acetylacetone, 0.2× water, and 27 mg of iodine. The electrophoretic setup consisted of a cathode (FTO glass) and an anode (titanium) immersed in the electrophoretic bath connected to a DC power supply. AST-P25 was deposited by applying 30 V for 20 s to deposit 4.0 ± 0.2 mg of AST-P25, which was then heated to 450 °C to improve the NP adhesion and remove organic impurities.

2.4. The preparation of stainless steel electrodes

The stainless steel (SS304) was cut into 9 × 9 mm squares, then ground with 600, 800, and finally 1200 fine grit silicon carbide paper. The squares were then polished well with a polishing pad using a 1 μm diamond spray at 250 rpm.

2.5. The preparation of base and welded 22MNB5 steel electrodes

A 200 × 100 mm coupon of galvanneal coated 22MNB5 Usibor® steel was heated in a baffle furnace at 900 °C for 6 min, then transferred to a press containing flat dies for press hardening. The cooling rate of the coupon during press hardening was in excess of 30 °C s^{-1} in order to achieve a fully martensitic microstructure. The samples were progressively ground to 600 grit size using silicon carbide paper. A single linear laser weld was performed using a fibre laser (IPG Photonics: YLS-6000) at a laser power and welding speed of 4 kW and 12 m min^{-1}, respectively. Welded specimens of 9 × 9 mm with the weld bead (1 mm diameter) in the centre were sheared from the coupon. For mass loss studies, an electrical wire was spot welded onto 22MNB5 steel samples and cold mounted using epoxy resin to isolate corrosion at one side of the coupon and prevent oxidation of the electrical wire contact. The other end of the electrical wire was connected to the photoanode.

2.6. Materials characterization

Raman spectroscopy was done with a Renishaw inVia microscope that has a 488 nm Ar ion laser. Powder XRD was done with a Rigaku SA-HF3 XRD with a Cu Kα radiation (1.54 Å) X-ray source (800 μm collimator, excitation voltage of 50 kV). The diffraction patterns were taken from 10° to 90° at 1.5° min^{-1}. HRTEM was done with a JEOL 2010F (Canadian Centre for Electron Microscopy, Hamilton, Ontario). EDS maps were collected for AST NPs and processed using Gatan Microscopy Suite: Digital Micrograph^{TM} (Ver. 2.11.1404.0) and ImageJ. Optical images of metal samples were collected on an Olympus BX51M optical microscope. Welded samples and cross-sections of corroded samples were etched in Nital (5 vol% nitric acid and 95 vol% ethanol) to reveal microstructural features. The etching time was 7 s by swabbing.

2.7. Photoelectrochemical and corrosion testing

Various experimental setups were used to determine SS304 corrosion performance with photoanode assisted cathodic protection and PEC properties of photoanodes. Both setups use a xenon solar simulator with either 400 nm cutoff or A.M. 1.5 G filters (Newport, Research Solar Simulator) and a Gamry Potentiostat (Series 300). The tests were conducted using Gamry Framework V4.35 software.

The PEC tests for photoanodes were done with a three-electrode setup immersed in an electrolyte contained in a quartz vessel. The working electrode (TiO₂ NPs on FTO glass), counter electrode (Pt mesh), and reference electrode (Ag/AgCl and saturated calomel) are connected to the potentiostat.

The galvanic cell used to test the corrosion of SS304 photoanodes consisted of a photoanode connected to a corrosion cell. The corrosion cell has a Pt counter electrode, SS304 working electrode, and a reference of SCE in 0.5 M NaCl, bubbled with nitrogen. The working electrode sample was housed in a Teflon holder so that only one side of the sample is exposed to the electrode solution and connected to the potentiostat. The photoanode cell has FTO glass coated with TiO₂ in a 0.2 M KOH
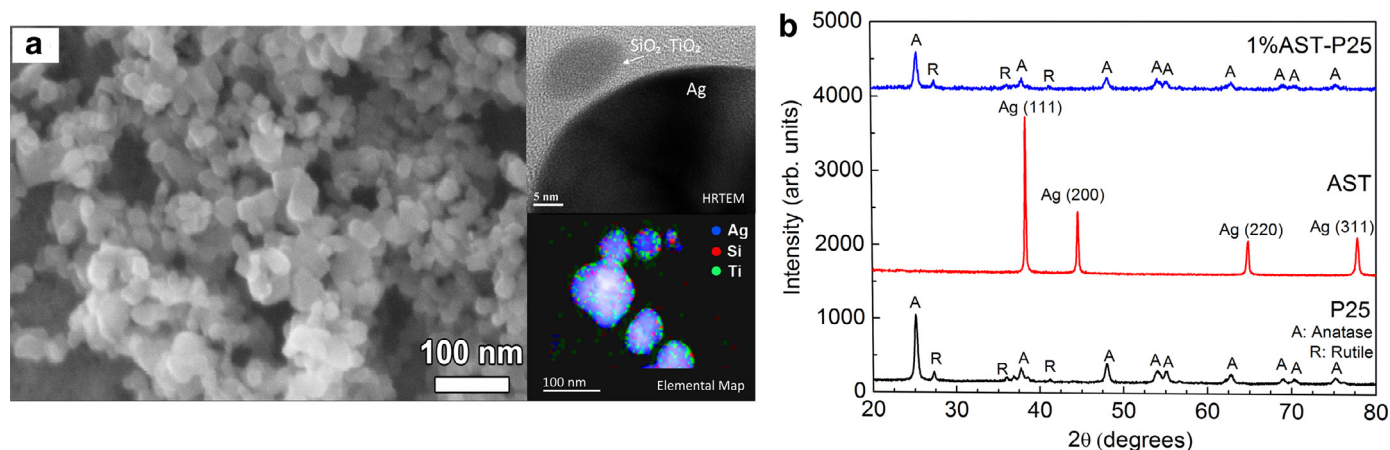
Fig.1. (a) An image of as-synthesized AST nanoparticles with superimposed HRTEM and EDX images, (b) an XRD spectra of AST-P25 composite and individual components.

solution. The two cells are connected between the SS304 steel and the AST-P25, as well as with a 1 M KCl electrolyte bridge.

The open circuit potential (OCP) test was done in both intermittent and continuous illumination, in open circuit mode for 10 h. In the hole scavenger studies, Na_2S and glucose was used as an inorganic and organic hole scavenger, respectively. The glucose concentration at various time points was determined using a colorimetric method reported elsewhere [30].

The cyclic potentiodynamic polarization and electroimpedance test was conducted with SS304 samples alone or connected to the photoanode under dark and continuous illumination. The potentiodynamic polarization test was used to determine the corrosion potential and current of the metal electrode. The test was scanned at 0.167 mV s^{-1}, from ± 0.150 V_{SCE} with respect to the V_{OCP}. Electrochemical impedance spectroscopy was used to determine the impedance arc generated by SS304 and was conducted under an AC sinusoidal wave of 5 mV without DC bias. The frequency examined was 100 kHz to 0.1 Hz at 10 points per decade. Nyquist and Bode plots were acquired from the impedance data.

The OCP and mass loss testing of 22MNB5 samples was similar to SS304 in that the corrosion cell was in 5 wt% NaCl and the PEC cell contained 0.1 M Na_2S. The 22MNB5 samples have higher carbon content (< 0.22 wt%) and will corrode faster than stainless steel 304 (< 0.08 wt%) (see Table S1). The test was maintained for 48 h. After the experiment, the solution was sonicated to remove loosely bound oxides. The samples were washed three times, then dried in a furnace at 100 °C overnight and weighed. Subsequently, the corrosion products were removed through washing and sonication in 0.1 M HCl. The sample was then rinsed with ultrapure water, dried in a furnace overnight, and weighed.

3. Results and discussion

3.1. Materials analysis

An SEM image of AST-P25 and TEM images of as-synthesized AST compounds are shown in Fig. 1. The Ag NPs developed by polyol methods are an average of 64.6 ± 12.3 nm. A thin layer of SiO_2 and TiO_2 around 10–15 nm can be seen by HRTEM. The Si and Ti seen in superimposed STEM-EDX images provide evidence of additional SiO_2–TiO_2. A mixture of AST and P25 sonicated in ethanol showed clustered P25 and AST NPs in SEM images.

3.2. The photoelectrochemical properties of the AST-P25 electrodes

For both P25 and AST-P25 electrodes, the photocurrent density of intermittent light (both unfiltered and filtered, < < 400 nm cutoff), was measured. For P25 it was determined to be 41 μm cm^{-2} and for AST-P25 it was determined to be 84 μm cm^{-2} (Fig.S1 in Supplementary information). The photocurrent density of AST-P25 under filtered (visible) light was determined to be 28 times greater than that of P25. The addition of Ag to the TiO_2 improves the photocatalytic efficiency with visible light. The surface plasmonic peak of Ag NPs is around 420 nm for synthesized NPs (see Fig. S2 in the Supplementary information) so the absorption peak coincides with the bandgap of TiO_2 allowing for visible light to generate photocurrent.

Glucose can reduce recombination and act as a hole scavenger. Glucose will adsorb onto the surface of the photocatalytic surface and will decompose via hole or hydroxyl attack at the interface under illumination. The photocurrent densities as a function of the glucose concentration was plotted and the curve corresponds to Langmuir kinetic models (see Fig. S1b in the Supplementary information). At high glucose concentrations, the reaction rate is governed by interfacial reactions because the photocurrent densities level off. At low glucose concentrations, mass transfer limits the reaction rate. The maximum photocurrent density, in 50 mM glucose, was determined to be 620 μA cm^{-2} under unfiltered xenon light illumination using AST-P25 photoanodes. The photocurrent density in glucose was 7.2 times that in 1 M KOH because of the oxidation reactions with glucose, which prevent electron–hole recombination.

3.3. Photocathodic protection of SS304 using AST-P25 photoanodes

The cathodic and anodic reaction processes will tend to equilibrium conditions. If electrons are withdrawn from metal, the rate of the anodic reaction and iron dissolution will increase, while the cathodic reaction will decrease. If electrons are supplied from an external source the anodic reactions will decrease to reduce corrosion. The corrosion current, I_{corr}, and the corrosion potential, E_{corr}, occur at the point of intersection of the anodic and cathodic curves (equilibrium). If electrons are injected into the metal, oxidation of iron is decreased to a potential E_{corr}' and the rate of the anodic current decreases to I_{corr}' due to an increase in the cathodic current.

Electroimpedance spectroscopy (Fig. S3) and potentiodynamic polarization (Fig. S4) were conducted with and without coupling with AST-P25 photoanodes in 5 wt% NaCl solution corrosion cell and 0.2 M KOH PEC cell under UV illumination. The corrosion potential of SS304 base metal (−0.258 V_{SCE}) was shifted to more negative potentials when SS304 was coupled with TiO_2 photoanode in the dark (−0.510 V_{SCE}) and under illumination (−0.970 V_{SCE}). I_{corr} increases when coupled under illumination, which may be attributed to enhanced electrochemical reaction at the interface arising from photogenerated electrons injected
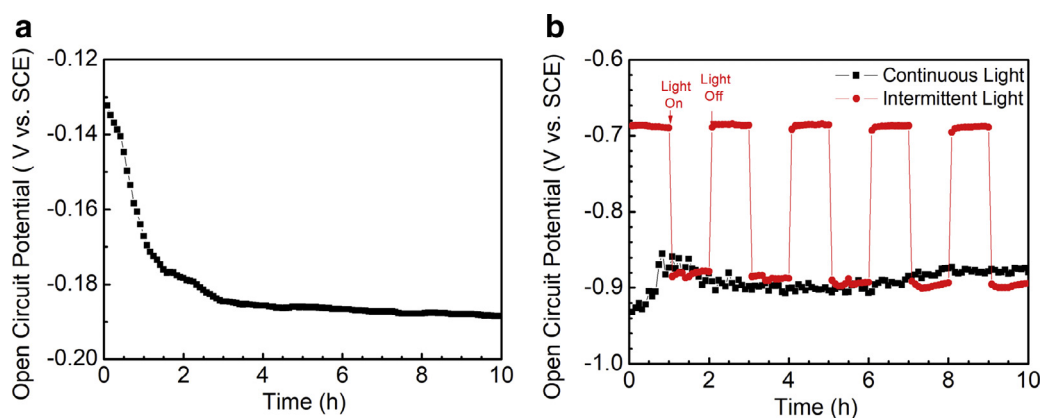
Fig. 2. The OCP over time for (a) an uncoupled SS304 electrode in a 0.5 M NaCl solution and (b) an SS304 and AST-P25 electrode in a 0.5 M NaCl solution with a 1 M KCl salt bridge and 0.2 M KOH with 0.1 M Na$_2$S in the photoanode cell.
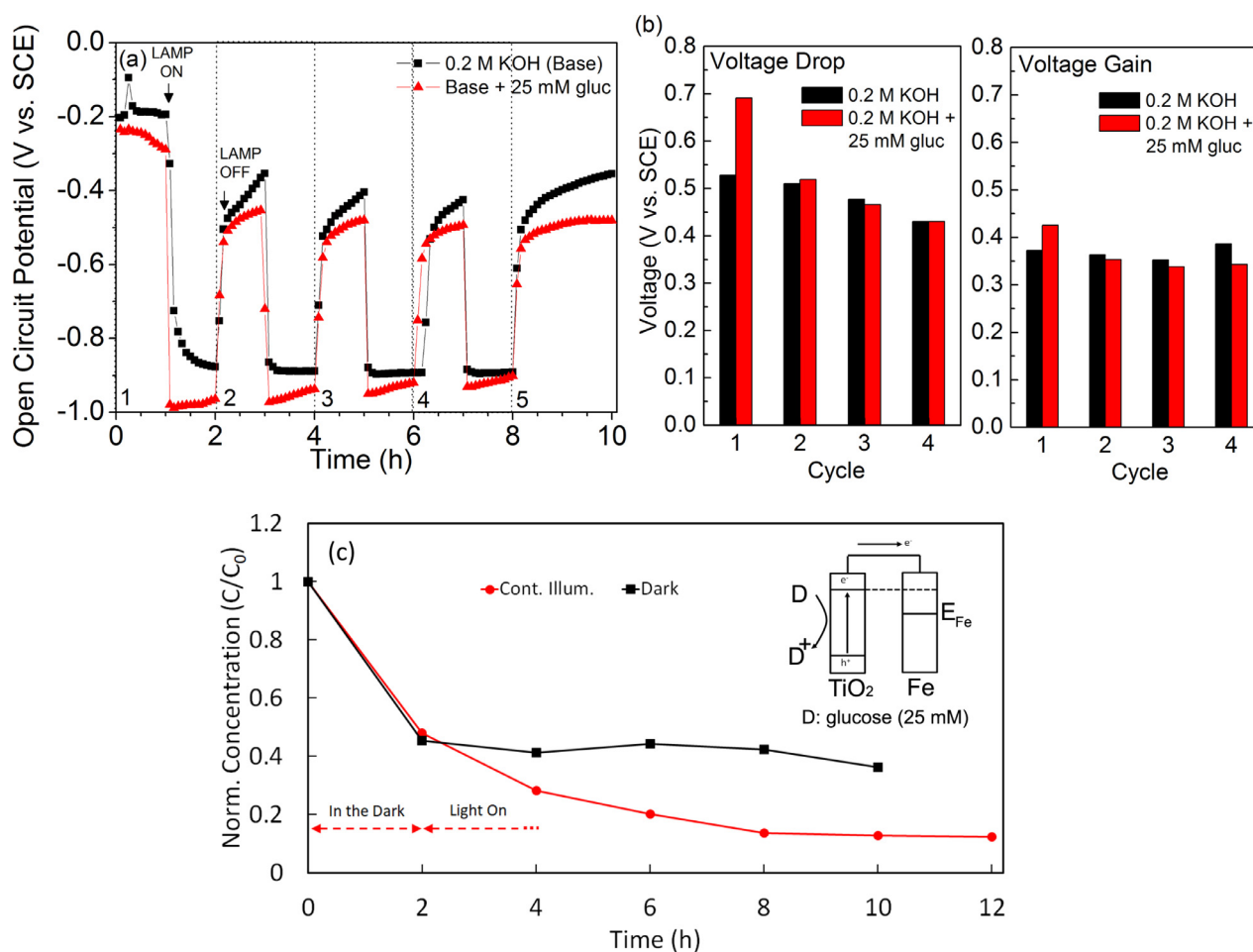

Fig. 3. (a) and (b), An SS304 electrode in 0.5 M NaCl and AST-P25 photoanode in 0.2 M KOH + 25 mM glucose, connected by a 1 M KCl salt bridge, under intermittent light. Normalized glucose concentration over time (c) under dark and light conditions.

into the SS304 metal. Nyquist plots indicated that the diameter of the impedance arcs of SS304 coupled with TiO$_2$ was much smaller than that of SS304 base metal with and without UV illumination due to the increase in photoelectrons at the interface of SS304.
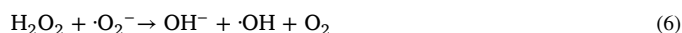
3.4. The effect of hole scavengers

Fig. 2(a) shows the OCP vs. time of an uncoupled SS304 electrode in 0.5 M NaCl solution, without the addition of a hole scavenger. As

seen in Fig. 2(b), the addition of a hole scavenger to the PEC cell can enhance the protection of SS304 from anodic corrosion reactions by reducing electron-hole recombination during photo-electron generation. The difference between the OCP in Fig. 2(a) and the OCP in Fig. 2(b) is the cathodic protection offered by AST-P25, which has an effect even when the light is off. The inorganic hole scavenger, Na$_2$S is dissociated into Na$^+$ and S^{2-} ions in aqueous solution. At the photoanode-electrolyte interface the S^{2-} ions in this reaction are sacrificial donors so the photocatalytic efficiency will decay over time [31].

The influence of glucose on the photocathodic protection of SS304 samples can be seen in Fig. 3(a). Adding glucose increases the magnitude of the OCP shift so it is more negative. When glucose is added under intermittent light the coupled potential of SS304 is decreased, and without light the potential increases. The increased potential suggests that partial protection of SS304 from anodic reactions is maintained. Over the course of the dark period, the potential decays to equilibrium. As seen in Fig. 3(b), the η decreases after each intermittent light cycle.

During the photocathodic process, the glucose will scavenge holes generated by the illuminated photoanode and oxidize over time (Fig. 3(c)). Approximately 60% and 90% of glucose is oxidized into its constituents under dark and solar irradiation. In the absence of light, glucose will establish an adsorption/desorption equilibrium with TiO_2. As seen in Fig. 3(c), this equilibrium is allowed to establish over a 2-h period for both samples in darkness, similar to previous tests in literature [32]. The extent of glucose binding in dark conditions has been previously linked to available surface area on the TiO_2 anode, which may vary due to differences in porosity [32] or differences in the surface area to glucose ratio. Afterwards, light is applied for the continuously illuminated sample and compared to a sample left in the dark. The oxidation of glucose under illumination matches well with the η decay after each intermittent cycle in Fig. 3(b), indicating the η is partially dependent on the glucose concentration in solution. In other words, photocathodic protection and organic degradation occur concurrently and the organic hole scavenger source must be replenished.

Irradiation of the TiO_2 catalyst generates hydroxyl radicals for organic contaminant degradation in aqueous solution by the following reactions:

$$TiO_2 + h\nu \rightarrow TiO_2\ (e^- + h^+) \tag{1}$$

$$OH^- + h^+ \rightarrow \cdot OH \tag{2}$$

$$O_2 + e^- \rightarrow \cdot O_2^- \tag{3}$$

$$O_2^- + H^+ \rightarrow \cdot HO_2 \tag{4}$$

$$2 \cdot HO_2 \rightarrow O_2 + H_2O_2 \tag{5}$$

$$H_2O_2 + \cdot O_2^- \rightarrow OH^- + \cdot OH + O_2 \tag{6}$$

Previous studies show that the photocatalytic degradation of glucose by TiO_2 results mainly in mineralization [33]. The other degradation products of glucose are arabinose and formic acid, as well as some fructose and erythrose [34]. Photocatalytic degradation of glucose starts with oxidation of the aldehyde to a carboxylic acid, then subsequent decarboxylation. An additional hydroxyl radical regenerates the aldehyde, producing a molecule of H_2O in the process. The carboxylic acid may also be lost as formic acid. The organic degradation products can undergo the same reactions to ultimately lose additional carbon atoms as either CO_2 or formic acid.
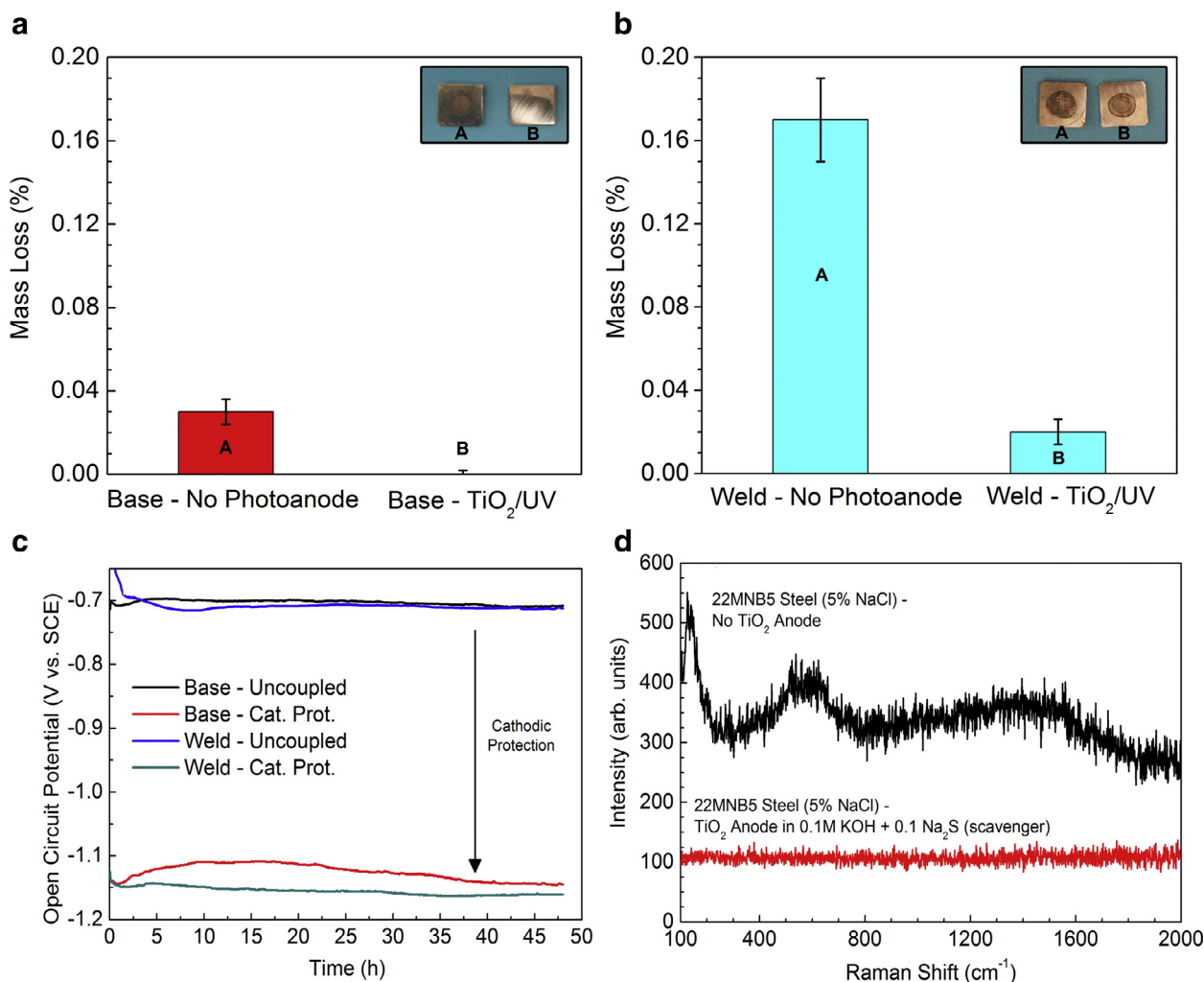

Fig. 4. Percentage mass loss of 22MNB5 steel of (a) base metal and (b) welded samples with and without TiO_2 photoanode under illumination after 48 h in 5% NaCl, as well as (c) open circuit potential and (d) Raman spectra of 22MNB5 steel with and without TiO_2/UV photocathodic protection.

3.5. Mass loss studies using corrosion-prone martensitic steel

Mass loss analysis was done on 22MNB5 base metal samples without photocathodic protection (Fig. 4(a)). The mass loss of 22MNB5 base metal without cathodic protection was 0.03% over 48 h. Under cathodic protection the mass loss was negligible. The TiO_2 photoanode has a higher negative potential under illumination, which indicates that the photoanode supplies electrons via semiconductor photocatalysis to the 22MNB5 base metal to prevent anodic reactions, which is observed visually in the negligible mass loss and mirror-like finish of the base metal coupon in Fig. 4(a). The negligible mass loss was also observed under Raman spectra analysis (Fig. 4(b)), which demonstrates lack of iron oxide peaks under cathodic protection and formation of iron oxide crystalline peaks without protection.

Welding of similar and dissimilar metals is required for water treatment infrastructure. The welding process changes the composition of the base metal [35] so there are galvanic couples formed from heterogeneous metal compositions, which will preferentially corrode the higher negative potential regions in the weld, heat-affected zone, and base metal(s) [36]. In this study, centre laser-welded 22MNB5 samples were used to test the corrosion performance under OCP (Fig. 4(c)). Introducing a weld onto the steel increased the mass loss of the uncoupled metal to 0.17% and a mass loss of 0.02% when coupling with the photoanode under UV illumination (Fig. 4(d)). The OCP behaviour with and without coupling of 22MNB5 welded samples was similar to the base metal because only a small region of the metal coupon was affected and the metal is predominantly of base metal composition. The formation of iron oxides under photocathodic protection for 22MNB5 welded samples is mitigated significantly when compared to the uncoupled case. The oxide formation on 22MNB5 welded samples are shown in Fig. S5. The figure clearly shows the location of the heat affected zone (HAZ) as the darker region between the fusion zone (FZ) and the base metal (BM), which is expected to be the area most susceptible to corrosion. This is apparent in the cross-sectional view of the corroded welded sample in which the HAZ is preferentially corroded first, since the depth of material removal is greatest in this region, followed by the FZ and then the BM.

4. Conclusions

Conventional cathode protection requires either a constant supply of external power or periodic replacement of a sacrificial anode. AST-P25 NPs were synthesized and demonstrated higher visible light photoactivity than commercial P25 alone under photoelectrochemical studies. AST-P25 NP coated electrodes demonstrated higher photocurrents under both filtered and unfiltered xenon lamp illumination. Inorganic and organic hole scavengers can be used to limit recombination and increase photocurrent supplied to the metal. Organic hole scavengers such as glucose can also be oxidized at the TiO_2 photoanode simultaneously as photoelectrons are injected to the metal cathode to prevent anodic reactions and electron–hole recombination. In addition, welded 22MNB5 samples corroded at a faster rate than base metal 22MNB5 samples, specifically at the HAZ. Using photocathodic protection, the mass loss from corrosion processes and surface oxidation was minimized.

Declaration of interest

The authors have no competing interests to declare.

Supplementary materials

Supplementary material associated with this article can be found, in the online version, at doi:10.1016/j.mtla.2018.08.033.

References

[1] European Federation of Corrosion, A Working Party Report on Sea Water Corrosion of Stainless Steels Mechanisms and Experiences, Institute of Materials, London, 1996.
[2] European Federation of Corrosion, A Working Party Report on Marine Corrosion of Stainless Steels Chlorination and Microbial Effects, Institute of Materials, London, 1993.
[3] D. Feron, Marine Corrosion of Stainless Steels, IOM Communications, for the European Federation of Corrosion, London, 2001.
[4] M. Kraljić, Z. Mandić, L. Duić, Corros. Sci. 45 (2003) 181–198.
[5] G.X. Shen, Y.C. Chen, L. Lin, C.J. Lin, D. Scantlebury, Electrochim. Acta 50 (2005) 5083–5089.
[6] J. Gallardo, P. Galliano, A. Durán, J. Sol-Gel Sci. Technol. 21 (2001) 65–74.
[7] A. Yağan, N. Özçiçek Pekmez, A. Yıldız, Electrochim. Acta 53 (2008) 2474–2482.
[8] D.A. Jones, Principles and Prevention of Corrosion, Prentice Hall, 1996.
[9] J. Yuan, S. Tsujikawa, J. Electrochem. Soc. 142 (1995) 3444.
[10] Y. Ohko, S. Saitoh, T. Tatsuma, A. Fujishima, J. Electrochem. Soc. 148 (2001) B24.
[11] T. Tatsuma, S. Saitoh, Y. Ohko, A. Fujishima, Chem. Mater. 13 (2001) 2838–2842.
[12] R. Liang, L.C.M. Li Chun Fong, M.J. Arlos, J. Van Leeuwen, E. Shahnam, P. Peng, M.R. Servos, Y.N. Zhou, J. Environ. Chem. Eng. 5 (2017) 4365–4373.
[13] M. Pelaez, N.T. Nolan, S.C. Pillai, M.K. Seery, P. Falaras, A.G. Kontos, P.S.M. Dunlop, J.W.J. Hamilton, J.A. Byrne, K. O'Shea, M.H. Entezari, D.D. Dionysiou, Appl. Catal. B Environ. 125 (2012) 331–349.
[14] A. Tong, R. Braund, D. Warren, B. Peake, Open Chem. 10 (2012).
[15] R. Liang, A. Hu, W. Li, Y.N. Zhou, J. Nanoparticle Res. 15 (2013) 1990.
[16] G. Laera, B. Jin, H. Zhu, A. Lopez, Catal. Today 161 (2011) 147–152.
[17] M.J. Arlos, M.M. Hatat-Fraile, R. Liang, L.M. Bragg, N.Y. Zhou, S.A. Andrews, M.R. Servos, Water Res. 101 (2016) 351–361.
[18] T. Hirakawa, P.V. Kamat, J. Am. Chem. Soc. 127 (2005) 3928–3934.
[19] J. Yu, L. Qi, M. Jaroniec, J. Phys. Chem. C 114 (2010) 13118–13125.
[20] H. Li, Z. Bian, J. Zhu, Y. Huo, H. Li, Y. Lu, J. Am. Chem. Soc. 129 (2007) 4538–4539.
[21] R. Liang, A. Hu, J. Persic, Y. Norman Zhou, Nano-Micro Lett. 5 (2013) 202–212.
[22] M.A. Butkus, M.P. Labare, J.A. Starke, K. Moon, M. Talbot, Appl. Environ. Microbiol. 70 (2004) 2848–2853.
[23] C.C. Levard, E.M. Hotze, G. V Lowry, G.E. † Brown, (2012).
[24] M.K. Kumar, S. Krishnamoorthy, L.K. Tan, S.Y. Chiam, S. Tripathy, H. Gao, ACS Catal. 1 (2011) 300–308.
[25] K. Awazu, M. Fujimaki, C. Rockstuhl, J. Tominaga, H. Murakami, Y. Ohki, N. Yoshida, T. Watanabe, J. Am. Chem. Soc. 130 (2008) 1676–1680.
[26] E. Angelini, S. Grassini, G.M. Ingo, D. Mombello, F. Fracassi, F. Palumbo, Surf. Interface Anal. 42 (2010) 666–670.
[27] S. Al Tarazi, L. Volpe, L. Antonelli, R. Jafer, D. Batani, A. D'esposito, M. Vitobello, Radiat. Eff. Defects Solids 169 (2014) 217–224.
[28] R. Liang, M. Hatat-Fraile, H. He, M. Arlos, M.R. Servos, Y.N. Zhou, SPIE Nanoscience Engineering, International Society for Optics and Photonics, 2015, p. 95450M.
[29] X. Zhang, Y. Zhu, X. Yang, S. Wang, J. Shen, B. Lin, C. Li, Nanoscale 5 (2013) 3359.
[30] A.-M.G. Vasilarou, C.A. Georgiou, J. Chem. Educ. 77 (2000) 1327.
[31] H.K. Jun, M.A. Careem, A.K. Arof, Int. J. Photoenergy 2013 (2013) 1–10.
[32] M. Maletić, M. Vukčević, A. Kalijadis, I. Janković-Častvan, A. Dapčević, Z. Laušević, M. Laušević, Arab. J. Chem. (2016).
[33] J.C. Colmenares, A. Magdziarz, A. Bielejewska, Bioresour. Technol. (2011) 11254–11257.
[34] M. Bellardita, E.I. Garcíagarcía-L´Opez, G. Marc'ı, M. Marc'ı, B. Megna, F.R. Pomilla, L. Palmisano, RSC Adv. 5 (2015).
[35] T.G. Gooch, Weld. Res. Suppl. Weld. J. (1996).
[36] S. Bakour, A. Guenbour, A. Bellaouchou, C. Escrivà-Cerdán, R. Sánchez-Tovar, R. Leiva-García, J. García-Antón, Int. J. Electrochem. Sci. 7 (2012) 10530–10543.